SPECIAL
Jets and Annular Structures in Geophysical Fluids
COLLECTION

Formation of Jets by Baroclinic Instability on Gas Planet Atmospheres

YOHAI KASPI AND GLENN R. FLIERL

Department of Earth, Atmospheric and Planetary Sciences, Massachusetts Institute of Technology, Cambridge, Massachusetts

(Manuscript received 21 June 2006, in final form 29 November 2006)

ABSTRACT

In this paper it is proposed that baroclinic instability of even a weak shear may play an important role in the generation and stability of the strong zonal jets observed in the atmospheres of the giant planets. The atmosphere is modeled as a two-layer structure, where the upper layer is a standard quasigeostrophic layer on a β plane and the lower layer is parameterized to represent a deep interior convective columnar structure using a negative β plane as in Ingersoll and Pollard. Linear stability theory predicts that the high wavenumber perturbations will be the dominant unstable modes for a small vertical wind shear like that inferred from observations. Here a nonlinear analytical model is developed that is truncated to one growing mode that exhibits a multiple jet meridional structure, driven by the nonlinear interaction between the eddies. In the weakly supercritical limit, this model agrees with previous weakly nonlinear theory, but it can be explored beyond this limit allowing the multiple jet–induced zonal flow to be stronger than the eddy field. Calculations with a fully nonlinear pseudospectral model produce stable meridional multijet structures when beginning from a random potential vorticity perturbation field. The instability removes energy from the background weak baroclinic shear and generates turbulent eddies that undergo an inverse energy cascade and form multijet zonal winds. The jets are the dominant feature in the instantaneous upper-layer flow, with the eddies being relatively weak. The jets scale with the Rhines length, but are strong enough to violate the barotropic stability criterion. It is shown that the basic physical mechanism for the generation and stability of the jets in the full numerical model is similar to that of the truncated model.

1. Introduction

Strong zonal winds dominate the atmospheres of the four big outer planets of the solar system. All four planets exhibit latitudinal banding and strong jet streams, where the wind velocities on Saturn are the strongest reaching more than 400 m s^{-1} near the equator, and Jupiter has the most structure with at least six alternating bands of east–west winds in each hemisphere (Ingersoll 1990; Porco et al. 2003). Unlike Earth, the solid centers are small fractions of the giant planets, the internal heat flux is almost as strong as the solar heat flux (except for Uranus), and the upper-atmosphere meridional temperature gradient is very weak. Consequently baroclinic instability has been assumed to play a minor role in the generation of these jets. However we show that even a weak baroclinic shear can result in substantial zonal flows that are stronger than the eddy field, and moreover baroclinic instability introduces a strong meridional variability in the velocity field. The instability acts as an energy source for the eddies, and the nonlinear eddy–mean interactions act to stabilize the flow.

Two general approaches have been taken to explain the strong zonal jets on the Jovian atmospheres. Busse (1976), inspired by the Taylor–Proudman effect, suggested that if the flow is deep and extends all the way through the planet, then the jets may be the surface manifestation of differentially rotating cylinders concentric with the planet's rotating axis. On the other hand, geostrophic turbulence theory (Rhines 1975, 1979), under the assumption that the dynamics are confined to an outer weather layer, suggests that the zonal jets emerge from decaying or stochastically forced turbulence on a β plane. The first to apply the shallow approach to Jupiter was Williams (1978, 1979) who used both barotropic and baroclinic models to show that an imposed turbulent eddy field can lead to an inverse energy cascade leading to jets on the order of

---

Corresponding author address: Yohai Kaspi, Department of Earth, Atmospheric and Planetary Sciences, Massachusetts Institute of Technology, Rm. 54-1417, Cambridge, MA 02139.
E-mail: yohai@mit.edu

DOI: 10.1175/JAS4009.1

the Rhines scale. Other authors have studied zonal jets appearing from geostrophic turbulence (Cho and Polvani 1996; Huang et al. 2001; Huang and Robinson 1998; Lee 2005; Manifori and Young 1999; Smith 2004; Vallis and Maltrud 1993). Panetta (1993) showed that jets can emerge from baroclinic instability in a two-layer model that has an imposed thermal gradient. This model allows transfer of energy from the upper to the lower layer and results in an equivalent barotropic jet. These jets seem persistent and stable, however they appear primarily when averaged, while the instantaneous fields are dominated by the eddies. Williams (2003) has produced jets in a baroclinic primitive equation system on a sphere and shows that, depending on details of the stratification and shear, the jets can migrate equatorward. Cho and Polvani (1996) show that in a shallow water layer on a sphere an eddy field evolves freely to a set of zonal jets at the lower latitudes. Using a barotropic vorticity model with small-scale random forcing and large-scale friction Huang et al. (2001) and Galperin et al. (2001) suggest a scaling law to the energy spectra of the jets and show (Galperin et al. 2001, 2006) that it matches the spectrum of the observed jets on Jupiter. Smith (2004) shows multiple jets emerging from stochastically forced quasigeostrophic (QG) turbulence in an equivalent barotropic system.

As applied to a gas giant's atmosphere, these shallow water or quasigeostrophic models have several flaws exemplified by comparison to Jupiter: first, the observed winds violate the barotropic stability condition (Ingersoll et al. 1981), thus $\beta - u_{yy} < 0$ at some latitudes, although the zonal winds appear to be very stable. In contrast, all of the models produce curvatures u_{yy}, which are smaller than β, so that the predicted jets are weaker or wider than the Jovian ones. Second, these shallow models assume a boundary at a depth of about one scale height, with the fluid below being motionless. But the thermal wind shear observed on Jupiter (Conrath et al. 1981; Gierasch et al. 1986) suggests that the flows will extend deeper and may increase, rather than die out, with depth. The Galileo probe showed exactly this kind of velocity structure (Atkinson et al. 1996), implying two separate regimes; an upper radiative regime (above 4 bars) and an inner deep adiabatic regime below. Third, these models either require random forcing or deal with decay of strong initial perturbations, leaving it unclear how such a state can be maintained. The exceptions, Panetta's (1993) and Williams' (2003) baroclinic instability models, require large-scale baroclinicity strong enough to satisfy the Charney–Stern theorem, so that turbulence can be generated and maintained by feeding on the available potential energy. But the observed global-scale temperature differences (Hanel et al. 1981, 1983; Ingersoll 1976) seem to be much smaller. Finally, for Jupiter, Saturn, and Neptune, the internal heat flux is estimated to be 0.67, 0.78, and 1.3 times, respectively, as strong as the absorbed heat flux from the sun (Hanel et al. 1981, 1983; Pearl and Conrath 1991); the shallow models do not attempt to account for the heat balance.

The deep approach assumes that the jet's generation comes from the interior of the planet, where the internal heat drives convection, which creates Taylor columns that penetrate throughout the planet, and therefore there is no confinement to a thin spherical shell. The assumption is that, since the planet is heated from within, convection drives it close to an adiabatic state and the Brunt–Väisälä frequency becomes much smaller than the rotation frequency leading to an interior Taylor column structure. Inspired by laboratory experiments (Busse 1970) where a homogeneous rapidly rotating sphere was heated from the inside and such a multicolumn structure was formed, Busse (1976, 1994) suggested that the interior of a planet may be occupied by Taylor columns that surround a hot core. He suggested that the multilayered structure of convection rolls might produce the zonal jets through nonlinear interactions among the columns. Numerical 3D models (Aurnou and Olson 2001; Christensen 2002; Sun et al. 1993) have demonstrated such Busse-type convection rolls in a homogeneous fluid can interact to produce zonal jets in a rapidly rotating system. Zhang and Schubert (1996, 1997) have showed that for a thermally driven convective interior, bounded by a corotating convectively stable stratified layer, the fluid motions resulting from the instability concentrate primarily in the outer stable region. Multiple band structures, which result from columnar convection, have been shown experimentally by Manneville and Olson (1996) though these bands occupy region only within 45° from the equator. Recently, Heimpel et al. (2005), using a model covering one-tenth the depth of the planet, have produced stable high-latitude jets driven by internal convection.

The spherical shape of the planet will cause deep penetrating Taylor columns moving toward the axis of rotation to stretch. This is in contrast to columns in an outer shallow-water layer in which the columns shrink as they approach the axis of rotation. This opposite effect suggests that such an inner geometry can be thought of as a negative β plane. Ingersoll and Pollard (1982) quantified this and developed a stability criterion for columnar motions inside of a compressible fluid sphere. Their equivalent barotropic stability equation has an effective β, which is negative and 3 times the value from the sphericity of the planet. On Jupiter and Saturn, the observed winds are close to marginal stability according to this criterion. Yano and Flierl (1994) have used this idea of a negative bottom layer β to demonstrate its effect on an isolated vortex like Jupiter's giant red spot in a zonal jet, and Yano (2005) used this to demonstrate that the equatorial jet will be prograde. We will show that having different and opposite-signed β values in the shallow and deep layer makes the dynamics quite different and favorable for creating jets even for weak baroclinic shears.

It is unclear how deep into the gas planet the zonal jets extend, but the *Galileo* entry probe found the winds on Jupiter to initially increase with depth and then become constant for as deep as they could be retrieved (up to the 24 bar level; Atkinson et al. 1996). Measurements of the temperature lapse rate (Seiff et al. 1996), suggest that between the levels of 5 and 16 bars the atmosphere is gravitationally stable, implying a possibly thicker outside nonconvective layer than previously assumed. This weakens previous theories that argued that the visible jets emerge solely due to the interaction between the convective cells. In addition, *Cassini* observations (Porco et al. 2003, 2005) have shown that the jets extend into high latitudes on both Jupiter and Saturn implying again that there may be an additional mechanism to the convection cells for the jet formation. Beyond a certain depth, however, convection is assumed to dominate (Guillot 1999), driving the system close to neutral stability. Therefore we shall analyze a model that contains elements of both the shallow and the deep approaches. The model is shallow in the sense that is quasigeostrophic and the jets are created by interactions of the eddies on a β plane. However, for the bottom layer, which represents the interior, we use the Ingersoll and Pollard (1982) parameterization for the deep convective interior. We hypothesize that the interaction between the isentropic interior and the weather layer drives the jets. We find that β and u_{yy} have similar values (thus the barotropic stability condition is violated) and still the jets are shown to be stable. Baroclinic instability provides an energy source, so that energy does not have to be pumped in to maintain the jets.

We begin with analysis of the stability problem in a two-layer quasigeostrophic model similar to the Phillips model (Phillips 1954), but with the lower layer deeper than the upper layer and having a different geometry represented by the different β. Unstable modes appear at high wavenumbers for low shears, implying there may be a significant scale separation between the eddies and the mean flows generated by the nonlinear interactions and the energy cascade. Next, since the fastest growing mode is the key contributor to the initial instability, we develop an analytical theory for the nonlinear problem containing of only this mode and zonal flow corrections. This truncated model, which is presented in section 4, gives an analytic expression for an induced zonal flow that has a multijet meridional structure, and that is not limited to the weakly supercritical case (Pedlosky 1970) so that it can be as strong as the eddies.

Then, using a pseudospectral fully nonlinear numerical model containing many initial modes, we show that indeed an induced zonal flow with a multijet meridional structure is generated from the baroclinic instability. The truncated model predicts well both the number of jets and their amplitudes. This emphasizes the importance of the truncated model, which allows us to isolate the physical mechanism of the jet formation before the system becomes turbulent. In time, as more unstable modes are generated, quasigeostrophic turbulence begins and an inverse energy cascade generates wider and stronger jets. Once the meridional scale of the jets has reached the Rhines scale, these jets become stable and in most cases have a bigger amplitude than the eddy field, thus creating a multijet structure across the whole channel. A complete description of the numerical experiments is given in section 5.

Previous models have shown that baroclinic instability can provide an energy source for a stable zonal jet structure (Panetta 1993). However in those cases the jets are obvious only in the zonally or time average profiles, while here the jets are seen in the instantaneous picture as well. A main difference is that in those models the scales of both the instability and the resulting jets are on the order of the deformation radius, while here there is a scale separation between the instability that is much smaller than the jets, which are again on the scale of the deformation radius. A few mechanisms govern the generation and stability of the zonal jets: baroclinic instability extracts energy from the basic shear at high wavenumbers to form small-scale eddies, eddy interaction creates an induced zonal flow with a strong meridional variation, and eddy–mean flow interaction creates exchange of energy between the eddies and the mean flow, which stabilizes the flow. The truncated model allows us to isolate these phenomena. Baroclinic instability tends to sharpen and intensify the jet once it is created while quasigeostrophic turbulence will tend to cascade the energy into larger scales. Both these effects can be seen in the numerical experiments. A discussion of these mechanisms and its relation to the Jovian jets is given in section 6.

2. The model

We use a two-layer quasigeostrophic model (Phillips 1954), with a simple shear flow on a β plane in a zonal channel of meridional width L. The layer thicknesses are different, such that the upper layer is much shallower than the lower layer, in order to represent a thin weather layer and a deep adiabatic interior. Although the two-layer model is often thought of as representing homogeneous incompressible fluids with the deep layer having a slightly larger density, Flierl (1992, 134–135) argues that an isentropic interior with a thin weather layer of higher entropy gives the same equations. To parameterize the deep-layer flows (Ingersoll and Pollard 1982), we use a negative β plane in the bottom layer and a standard β plane for the upper layer, as discussed in the introduction. The opposite-signed β's make the stability problem quite different from the classical case (Pedlosky 1987). There is a free interface between the two layers whose horizontal height gradient is related to the difference in pressure gradients within the layers. The quasigeostrophic inviscid potential vorticity equation for each layer, dimensionalized in the standard way as in Pedlosky (1987) is

$$\left(\frac{\partial}{\partial t}+\frac{\partial \Psi_n}{\partial x}\frac{\partial}{\partial y}-\frac{\partial \Psi_n}{\partial y}\frac{\partial}{\partial x}\right)[\nabla^2\Psi_n + (-1)^n F_n(\Psi_1-\Psi_2)+\beta_n y]=0, \tag{1}$$

where n denotes the layer, Ψ_n is the streamfunction, and F_n is the nondimensional Froude number given by

$$F_n=\frac{f^2L^2}{g'D_n}, \tag{2}$$

where f is the Coriolis parameter, g' is the reduced gravity, and D_n is the layer depth. For future notation we denote the full potential vorticity in each layer as

$$\Pi_n=\nabla^2\Psi_n+(-1)^nF_n(\Psi_1-\Psi_2)+\beta_n y. \tag{3}$$

We will assume the simplest basic state with a uniform flow in each layer,

$$\Psi_{0n}=-U_n y. \tag{4}$$

The total streamfunction is composed of the mean part (4) and a perturbation

$$\Psi_n=\Psi_{0n}+\phi_n \tag{5}$$

and the equation for the perturbation streamfunction is

$$\left(\frac{\partial}{\partial t}+U_n\frac{\partial}{\partial x}\right)q_n+[(-1)^nF_n(U_1-U_2)+\beta_n]\frac{\partial \phi_n}{\partial x}+J(\phi_n,q_n)=0, \tag{6}$$

where

$$q_n=\nabla^2\phi_n+(-1)^nF_n(\phi_1-\phi_2) \tag{7}$$

is the perturbation potential vorticity and $J(\phi_n, q_n)$ is the Jacobian of streamfunction and potential vorticity. The boundary conditions on the walls of the channel at $y = 0, 1$ are that the meridional velocity vanishes and the zonally averaged circulation on the two walls is conserved (Phillips 1954) so that

$$\frac{\partial \Psi_n}{\partial x}=0,\quad \frac{\partial}{\partial t}\int\frac{\partial \Psi_n}{\partial y}\,dx=0. \tag{8}$$

3. Linear stability analysis

We begin by addressing the linear stability problem in a similar fashion to Phillips (1954) and Pedlosky (1970). Wave solutions that satisfy the boundary conditions (8) can be found in the form

$$\phi_2=\gamma\phi_1=\gamma A e^{ik(x-ct)}\sin(m\pi y), \tag{9}$$

where m is an integer, k is the zonal wavenumber, A is the amplitude of the wave in the upper layer, and γ is the ratio between the amplitude of the perturbation in the lower to that of the upper layer. Only k is restricted to be real. Substituting (9) into (6) and solving the linear eigenvalue problem gives the dispersion relation

$$\begin{aligned}c={}&U_2+\frac{U_S}{2}\frac{\kappa^2+2F_2}{\kappa^2+F_1+F_2}-\frac{\beta_2(\kappa^2+F_1)+\beta_1(\kappa^2+F_2)}{2\kappa^2(\kappa^2+F_1+F_2)}\pm\frac{1}{2\kappa^2(\kappa^2+F_1+F_2)}\{U_S^2\kappa^4(\kappa^4-4F_1F_2)\\&+2U_S\kappa^2[(\beta_2-\beta_1)(\kappa^4-2F_1F_2)+\kappa^2(\beta_2F_1-\beta_1F_2)]+[(\kappa^2+F_1)\beta_2-(\kappa^2+F_2)\beta_1]^2+4F_1F_2\beta_1\beta_2\}^{1/2},\end{aligned} \tag{10}$$

where $U_S = U_1 - U_2$ and $\kappa^2 = k^2 + l^2$, where $l = m\pi$. The solution also gives an expression for the ratio between the perturbation amplitude in each layer

$$\gamma=1+\frac{\kappa^2}{F_1}-\frac{F_1U_S+\beta_1}{F_1(U_1-c)}. \tag{11}$$

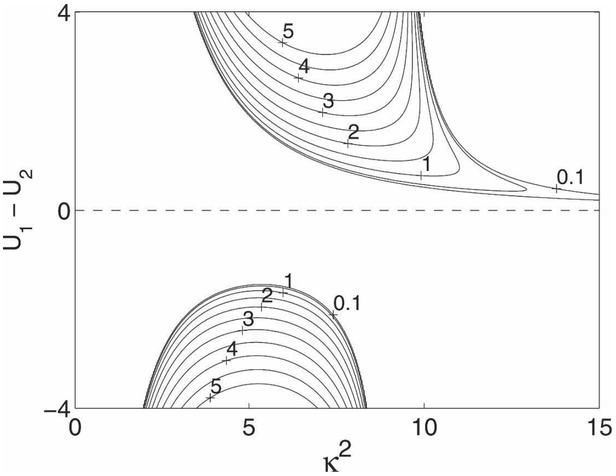

FIG. 1. Stability curves for the two-β case for the vertical shear as function of the total wavenumber. The contours are of the growth rate in nondimensional units, and the parameters used here are $F_1 = 100$, $F_2 = 20$, $\beta_1 = 10$, and $\beta_2 = -30$.

As seen in Fig. 1 the shortwave cutoff for classical two-layer baroclinic instabilities has disappeared and the marginal instability curve has a tail toward the high wavenumbers. This effect does not require the bottom layer β to be negative, only to differ from the upper one as shown by Steinsaltz (1987) for the case of a sloping bottom or by Robinson and McWilliams (1974) for a case of a varying bottom topography. However, the form of the potential vorticity (3) shows that for cases where the sign of β is different in the two layers, the necessary condition for instability can be reached for weak shears, and analysis of (10) shows that this tail asymptotes to zero shear as $k \to \infty$ (Fig. 1). Therefore, baroclinic instability may arise with the maximum growth rate at high wavenumbers even when the shear is very small. As seen in Fig. 1, the growth rate for a very small shear may itself be very small, and may seem insignificant, but since the observed zonal jets on the outer planets are long lived, an energy source from the weak instability may suffice.

The form of c (10) is symmetric in the meridional and zonal wavenumber. A priori, one might think that the lowest meridional wavenumber for a given shear will be the most unstable [since the growth rate is $kc_i(\kappa) = \sqrt{\kappa^2 - l^2}c_i(\kappa)$] so that the growth will not generate much meridional structure. However, the meridional wavenumbers must be quantized as multiples of π to satisfy the boundary condition in the channel, and for weak shears the band of unstable wavenumbers is thinner than π in wavenumber space. Thus for a given shear it may be that only high meridional wavenumbers are unstable. This is demonstrated in Fig. 2.

4. The nonlinear truncated model

The linear stability analysis implies that the shortwave perturbations will become dominant for weak shears. In relation to the Jovian jets this implies the possibility of baroclinic instability creating a highly varying meridional structure. Of course, this must be tested in a full numerical model, and obvious questions are: can this meridional variation evolve into zonal jets? And if so, are the zonal velocities stable over time? In section 5 we use a full nonlinear numerical model to test this. However, before doing that, we can get some insights by solving the nonlinear system truncated to a perturbation in one wavenumber. Although this restricts the nonlinear nature of the solution, the band of initial growing modes in the two β case is limited (Fig. 2), so that this solution actually reproduces quite well (Fig. 5) the initial stages of the fully nonlinear solution obtained numerically in section 5.

Therefore, we proceed to examine the nonlinear dynamics with taking the perturbation to have only one zonal wavenumber and one meridional wavenumber. Rewriting (6) in terms of the barotropic Π_T, Ψ_T, and baroclinic Π_C, Ψ_C components gives

$$\frac{\partial}{\partial t}\Pi_T + J(\Psi_T, \Pi_T) + J(\Psi_C, \Pi_C) = 0 \tag{12}$$

$$\frac{\partial}{\partial t}\Pi_C + J(\Psi_T + \xi\Psi_C, \Pi_C) + J(\Psi_C, \Pi_T) = 0, \tag{13}$$

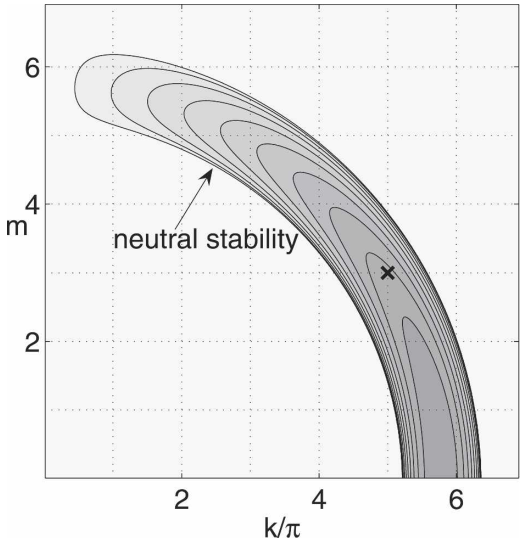

FIG. 2. Growth rates in horizontal wavenumber space for the two-β case. The x axis is the zonal wavenumber and the y axis is the meridional one (divided by π). The growth is confined to a band of few wavenumbers. Because of the boundary conditions, the fastest growing mode (in this case $k_m = 5$, $l_m = 3$, marked with ×) is not necessarily the gravest mode. The parameters used here are $F_1 = 100$, $F_2 = 50$, $\beta_1 = 10$, $\beta_2 = -30$, and $U_S = 0.153$.

where the barotropic and baroclinic components of the potential vorticity are

$$\Pi_T = \frac{\delta\Pi_1 + \Pi_2}{1 + \delta} \tag{14}$$

$$\Pi_C = \frac{\sqrt{\delta}}{1 + \delta}(\Pi_C - \Pi_T), \tag{15}$$

and $\delta = D_1/D_2$ is the layer depth ratio. The same structure applies for the barotropic and baroclinic streamfunctions Ψ_T and Ψ_C. The parameter $\xi = [(1 - \delta)/\sqrt{\delta}]$ comes from the unequal upper- and lower-layer thicknesses. Split into a basic state and a perturbation and using (3) and (4), the barotropic and baroclinic streamfunctions and potential vorticities are

$$\Psi_T = \phi_T \tag{16}$$

$$\Psi_C = -U_C y + \phi_C \tag{17}$$

$$\Pi_T = \frac{(\delta\beta_1 + \beta_2)y}{1 + \delta} + q_T \equiv Q_T y + q_T \tag{18}$$

$$\begin{aligned}\Pi_C &= \left[\frac{\sqrt{\delta}}{1 + \delta}(\beta_1 - \beta_2) + (F_1 + F_2)U_C\right]y + q_C\\ &\equiv Q_C y + q_C,\end{aligned} \tag{19}$$

where U_C is the baroclinic shear, and ϕ and q are the perturbation streamfunction and potential vorticity, respectively. Note that the basic-state barotropic streamfunction has been taken to be zero. This can be done due to the Galilean invariance of the two-layer system. Then the barotropic and baroclinic Eqs. (12), (13) take the form

$$\frac{\partial}{\partial t}q_T + U_C\frac{\partial}{\partial x}q_C + Q_T\frac{\partial}{\partial x}\phi_T + Q_C\frac{\partial}{\partial x}\phi_C + J(\phi_T, q_T) + J(\phi_C, q_C) = 0 \tag{20}$$

$$\frac{\partial}{\partial t}q_C + U_C\left(\frac{\partial}{\partial x}q_T + \xi\frac{\partial}{\partial x}q_C\right) + Q_T\frac{\partial}{\partial x}\phi_C + Q_C\left(\frac{\partial}{\partial x}\phi_T + \xi\frac{\partial}{\partial x}\phi_C\right) + J(\phi_T + \xi\phi_C, q_C) + J(\phi_C, q_T) = 0. \tag{21}$$

We express the solution as a single potential vorticity perturbation wave that satisfies the boundary conditions (8) of the form

$$q_T = q'_T(t)e^{ikx}\sin(ly) + \text{c.c.} \tag{22}$$

$$q_C = q'_C(t)e^{ikx}\sin(ly) + \text{c.c.}, \tag{23}$$

where c.c. is the complex conjugate, and then the perturbation stream functions can be expressed via inverting Eq. (7) so that

$$\phi_T = \frac{-q_T}{\kappa^2} \tag{24}$$

$$\phi_C = \frac{-q_C}{\kappa^2 + F_1 + F_2}. \tag{25}$$

The main advantage of writing the quasigeostrophic potential vorticity equations in this form is that when plugging (22)–(25) into (20), (21) the Jacobians from the barotropic Eq. (20) vanish, while the baroclinic nonlinear contribution (21) gives

$$\begin{aligned}&J(\phi_T, q_C) + J(\phi_C, q_T)\\ &\quad = \frac{ikl(F_1 + F_2)}{\kappa^2(\kappa^2 + F_1 + F_2)}(q'_C q'^*_T - q'^*_C q'_T)\sin(2ly).\end{aligned} \tag{26}$$

This is where the truncated nature of the solution appears. The nonlinear baroclinic interaction gives a zonal mean correction to the basic flow with a specific meridional structure which depends on the choice of the truncated mode. Nevertheless, as mentioned in the linear analysis (which applies when the perturbation is small) since the band of growing modes contains only few modes (Fig. 2) an approximation of only one growing mode turns out to be a fair approximation. Since the basic zonal flow is fixed, we can specify this mode to be the fastest growing mode. Therefore we can split the baroclinic Eq. (21) in two: one part for the linear perturbation, and another for the nonlinear correction. From the solution to the nonlinear part (26) we can approximate the structure of the nonlinear correction to the potential vorticity as having the form

$$\overline{q_C} = \overline{q'_C}(t)\sin(2ly). \tag{27}$$

This form is different than the linear perturbation part, (9), having no zonal dependence and a different me-

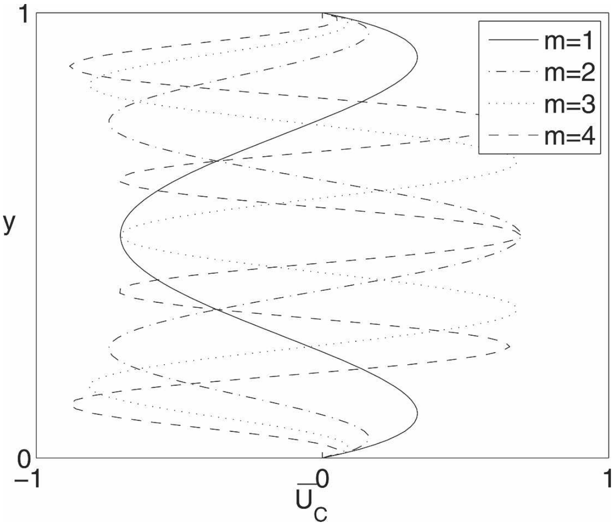

FIG. 3. The analytical baroclinic induced zonal velocity $\overline{U_C}$ [Eq. (29)] from the truncated model as function of the channel width for the first four meridional modes.

ridional structure. This nonlinear correction to the basic baroclinic state must also satisfy the two boundary conditions given by (8). To ensure this, we use the inversion relation from (7) for the zonally averaged case

$$\left[\frac{\partial^2}{\partial y^2} - (F_1 + F_2)\right]\overline{\phi_C} = \overline{q_C}, \qquad (28)$$

which, when solved for $\overline{\phi_C}$ with the boundary conditions, gives a correction to the basic zonal velocity

$$\overline{U_C} = \frac{2l\overline{q'_C}(t)}{4l^2 + F_1 + F_2} \times \left\{\cos(2ly) - \frac{\cosh\left[\sqrt{F_1 + F_2}\left(y - \frac{1}{2}\right)\right]}{\cosh\left(\frac{\sqrt{F_1 + F_2}}{2}\right)}\right\}. \qquad (29)$$

This result is similar in form to that found for the weakly nonlinear theory by Pedlosky (1970). Here though, the weakly nonlinear requirement is relaxed (but replaced by a truncation assumption) and this correction may extend into the highly supercritical regime, as we show in the numerical experiments in section 5. The amplitude of this zonal flow is not limited to the weakly varying parameter and, in fact, can be stronger than the eddies themselves.

Figure 3 shows the shape of the mean flow correction for the first few modes, and indicates that for the higher modes we expect to get a multijet meridional structure. This baroclinic contribution tends to reduce the shear rather than increase it, causing oscillations in the amplitude of the perturbation as in the classical weakly supercritical case (Pedlosky 1970), once the correction reduces the shear enough it goes back into the stable regime, halting the growth until the effect of the nonlinearities decreases, and the cycle repeats. Here, since the flow may be strongly rather than weakly supercritical the nonlinear wave effects may not be enough to halt the growth. For the cases of high wavenumber perturbations, though, the growth band (Fig. 2) becomes narrow in wave space so that the effect of the nonlinear correction is similar to that of the weakly nonlinear case, and the perturbation may reach a steady equilibrium. These oscillations can be seen in Fig. 4.

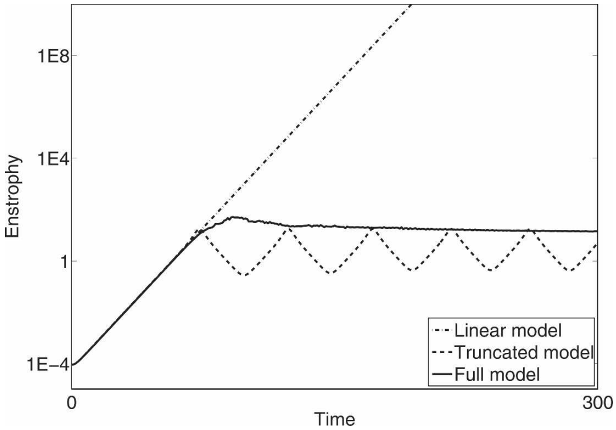

FIG. 4. The enstrophy as a function of time. The dash–dot line is the linear growth rate for the fastest growing mode using the linear growth rate from Eq. (10). The dashed line is the growth calculated from the truncated model [Eqs. (30) and (31)]. This shows that when the perturbation is small the system aligns with the linear growth rate, until the nonlinear terms become dominant and the system begins oscillating while exchanging energy between the eddies and the mean flow. The solid line is the result for the full nonlinear system (run S4), which qualitatively follows the truncated model but contains many modes and therefore does not have a pure oscillation.

The truncation and the separation of the nonlinear part out of the baroclinic equation allows us not only to find the baroclinic-induced zonal velocity $\overline{U_C}$, but to solve for the perturbation amplitudes and the baroclinic mean. We can write the truncated system as a closed system of three equations for three unknowns: the perturbation amplitudes q'_T, q'_C and the baroclinic mean $\overline{q'_C}$. The specifics of this derivation are given in the appendix. The resulting system is

$$\frac{\partial}{\partial t}\mathbf{q} + ik\mathbf{L}\mathbf{q} + ik\overline{q'_C}\mathbf{N}\mathbf{q} = 0 \qquad (30)$$

$$\frac{\partial}{\partial t}\overline{q'_C} + \frac{ikl(F_1 + F_2)}{\kappa^2(\kappa^2 + F_1 + F_2)}(q'_C q'^*_T - q'^*_C q'_T) = 0, \qquad (31)$$

where $\mathbf{q} = \begin{pmatrix} q'_T \\ q'_C \end{pmatrix}$, and the operators $\mathbf{N}$ and $\mathbf{L}$ are given in the appendix as well. This solution is shown in Fig. 4, which plots the evolution of enstrophy in time for the linear case, the truncated nonlinear case, and a full nonlinear model containing many modes (section 5). This example shows how the nonlinearities stabilize the initial instability in both the truncated and full model.

Since the initial perturbation is small, and the system is baroclinically unstable, the perturbations in all models grow similarly. When the effect of the nonlinearities is large enough, the nonlinear models separate from the linear model and, since the perturbation is dominated by the most rapidly growing mode, the truncated model with only this mode gives a reasonable estimate of this separation point. Then the truncated model begins to oscillate by exchanging energy between the perturbations and the basic flow, whereas the full model (which resolves harmonics neglected in the truncation) equilibrates with a much more steady amplitude. In general, this truncated solution captures well when, where, and how the interaction with the mean flow halts the instability.

In summary, the truncated model allows us to examine qualitatively the nonlinear interactions, which have several roles. First, they create an induced zonal flow with a highly varying meridional structure, which (as we show in section 5) may be stronger than the eddies and therefore have the potential of becoming zonal jets. Second, this induced flow stabilizes the growing perturbations. This toy model provides a closed system of equations for the perturbation amplitude in both layers and the change in the basic flow due to nonlinearities, without requiring the system to be only slightly supercritical; for such cases the correction due to the nonlinearities becomes significant (as opposed to being on the order of the departure from the critical curve) and a strong multijet structure may emerge. Indeed, since the high wavenumber instability dominates the two-β case, we might expect multiple jets for a weak baroclinic shear.

5. Fully nonlinear model and the generation of high modal jets

The truncated model predicts a multijet structure for high wavenumber instability. In this section we use a fully nonlinear numerical model to explore the role of the other modes on the generation of eddies and jets, and on the effect of quasigeostrophic turbulence on these jets. The model we use is based on the same equations analyzed in the previous sections. It is pseudospectral (Boyd 2001), where each layer has a spatial resolution of 64 × 128, is periodic in the zonal direction, and is confined within a channel in the meridional direction. On the channel walls we require no meridional flow and that the circulation is conserved (implemented by requiring the mean ageostrophic meridional velocity to vanish).

The parameter regime is fairly simple since we only set the layer depths (by setting the nondimensional Froude numbers), the β parameters and the baroclinic shear. If we were to fully compare the numerical model to the truncated model we would set the shear in such a way that only one mode will be growing (see Fig. 2). For our standard run, following Dowling and Ingersoll (1989) and Ingersoll and Pollard (1982) we choose the typical Rossby deformation radius to be on the order of 2000 km. This value corresponds to the observed scale of the jets on Jupiter. We take the domain width to be an order of magnitude bigger than the deformation radius, thus setting the upper nondimensional Froude number to be $F_1 = 100[F_n = (L^2/L_D^2)]$. The bottom layer is taken as to be 5 times as deep so that $F_2 = 20$; β_1 is set according to the curvature of Jupiter $[\beta_1 = (2\Omega \cos\theta/R_J)(L^2/U)]$, giving the nondimensional value $\beta_1 = 10$, with the characteristic velocity being 50 m s^{-1} and the same typical horizontal length scale of 2×10^4 km. Following the barotropic stability analysis by Ingersoll and Pollard (1982), which shows that β_2 is at least $-3\beta_1$ we set β_2 to this value. Their analysis shows that this is a lower limit for stability and in fact a more negative lower-layer β will be stable, but for our standard run we choose this limit. Unlike other models for jets (Panetta 1993; Vallis and Maltrud 1993; Williams 1979) we find in the upper layer that the standard barotropic stability criterion (Kuo 1949) is violated (Fig. 13), much as we see in the observations, but the flow is still stable. We refer to these values as our standard run (denoted with S and the run number—see Table 1), and experiment sets B and F show a sensitivity analysis to the parameters of the standard run. The vertical shear is set so that several growing unstable modes exist, as demonstrated in Figs. 1 and 2. Since the two-layer model is Galilean invariant (Pedlosky 1987) it is only necessary to set the baroclinic shear, and not the absolute values of the basic-state velocities.

We begin all our experiments with a small random potential vorticity perturbation field, with initial perturbations in all π multiple wavenumbers up to k, $l = 10\pi$. Since the system is forced by a constant vertical shear, eventually the system becomes baroclinically unstable and the fastest growing mode dominates. We denote this fastest growing mode with the notation k_m,

TABLE 1. Numerical experiments using the fully nonlinear pseudospectral model, where F_1 is the Froude number for the upper layer; δ is the layer depth ratio between the upper and lower layer (and inverse of the Froude number ratio); β_1 is the β-plane parameter for the upper layer; B is the ratio β_2/β_1; U_S is the imposed vertical shear; k_m, l_m are the fastest growing baroclinic modes; λ is the meridional spectral maximum of the statistically steady state averaged across the channel (thus $1/\lambda$ gives an estimate for the average number of jets), and η is the ratio of the induced zonal velocity amplitude to the eddy amplitude (see text) in each layer.

Run	F_1	$1/\delta$	β_1	B	U_S	k_m, l_m	$1/\lambda$	η_1	η_2
S1	100	5	10	−3	0.0263	10, 8	7	1.87	0.11
S2					0.0296	9, 8	8.9	2.32	0.13
S3					0.0332	9, 7	6.37	3.1	0.15
S4					0.0338	8, 7	7.09	3.17	0.13
S5					0.0372	10, 4	6.25	3.33	0.13
S6					0.0385	8, 7	5.79	2.54	0.17
S7					0.0413	10, 3	7.53	1.56	0.11
S8					0.044	8, 6	5.44	3.18	0.25
S9					0.045	8, 7	7.71	3.46	0.15
S10					0.0455	9, 4	4.14	3.26	0.17
S11					0.0494	8, 4	6.88	3.07	0.19
S12					0.05	9, 3	6.14	1.35	0.14
S13					0.0525	9, 2	4.28	3.2	0.28
S14					0.0562	8, 4	6.5	2.94	0.22
S15					0.0612	7, 5	6.92	1.94	0.36
S16					0.0622	8, 3	5.63	2.36	0.31
S17					0.0632	7, 3	5.76	2.07	0.25
B1	100	5	10	−10	0.1032	10, 4	8.56	2.27	0.1
B2				−5	0.056	10, 4	7.33	1.83	0.11
B3				−2	0.0277	9, 6	7.26	1.63	0.15
B4				−1	0.0183	9, 6	5.92	0.73	0.16
B5				0	0.0088	None	No jets	0	0
B6				1	0.0006	None	No jets	0	0
F1	100	1	10	−3	0.0382	10, 4	6.15	0.48	0.21
F2		10			0.037	9, 7	10.25	2.78	0.11
F3		100			0.0369	8, 5	6.04	0.51	0.03

l_m such that $k = k_m\pi$ and $l = l_m\pi$. As seen in Fig. 4 the enstrophy begins growing in agreement with linear theory (since the amplitude is small). When the effects of nonlinearity grow enough, the enstrophy diverges from the theoretical linear growth curve as predicted by the truncated model. It can be seen that the nonlinear truncated model predicts quite precisely where this separation takes place. Moreover, when we plot a snapshot of the top layer induced zonal flow $\overline{U_1}$ at the time when the linear and nonlinear models diverge from the numerical experiments (circles in Fig. 5), it matches well the truncated model analytic prediction. The reason for this is that as long as the growth of the perturbation is dominated by the fastest growing mode according to the truncated model there is no induced barotropic velocity. From the form of (14), (15) we can write the induced zonal velocity in each layer

$$\overline{U_1} = \frac{1}{\sqrt{\delta}}\overline{U_C} + \overline{U_T} \quad \overline{U_2} = -\sqrt{\delta}\,\overline{U_C} + \overline{U_T} \tag{32}$$

and therefore the induced zonal flow in each layer has the same meridional structure as the baroclinic induced zonal flow $\overline{U_C}$. We see exactly a ratio of δ between of the amplitude of the induced zonal flow in the upper and lower layers.

In Fig. 5 the analytic result of Eq. (29) is plotted for the cases of meridional wavenumbers $m = 4, 8$ with the results from the full model for runs S2 and S14. The numerical results contain 65 points (the meridional resolution of the model) and are a snapshot of $\overline{U_1}$ [which has the same structure as the $\overline{U_C}$ field (32)] taken just before the time when the two models diverge. Therefore, although the choice of only one mode in the truncated model seems initially quite restrictive for a nonlinear prediction, in this type of instability scenario where the fastest growing mode dominates until turbulence develops, the truncation is quite useful. After the models diverge and more modes come into play, the truncated and the full numerical models differ in the sense that there is no pure oscillation in enstrophy in the full model as in the truncated model (although we can create such oscillations for special weakly nonlinear cases), but rather a noisier signal (Fig. 4). However, the amplitude in the two models is of

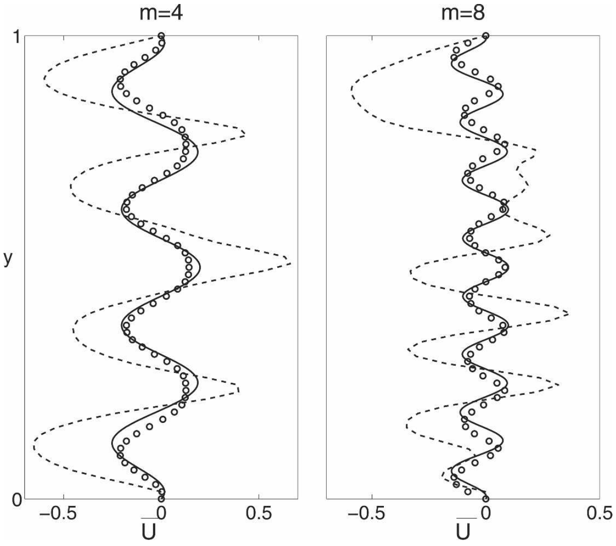

FIG. 5. The induced zonal velocity as a function of the channel width for runs S2 and S14. The solid line is the analytic baroclinic correction $\overline{U_C}$ [Eq. (29)] from the truncated model; the circles are the result from the nonlinear numerical model (the 65 points are the meridional resolution of the grid) toward the end of the baroclinic growth stage for $\overline{U_1}$, and the dashed line is the zonally averaged steady-state zonal velocity from the numerical results after the inverse energy cascade.

the same order. Qualitatively, this equilibrium state is the same as seen in the truncated model for one mode, except that, as the energy cascades more modes appear, and the combination of them all creates this leveling of the enstrophy. Figure 5 then also shows the final steady state after the inverse cascade, showing distinct jets with a scale set by the baroclinic induced zonal velocity $\overline{U_C}$. The jets have sharper eastward than westward winds, because of the asymmetry in the barotropic stability criterion (Fig. 13).

The total zonal velocity in each layer is composed of three components: the constant basic flow creating the vertical shear, the induced zonal velocity created by the nonlinear interaction $\overline{U_n}$ and the u_n' eddy field. As the instability grows, the induced zonal flow grows by many orders of magnitude and, as discussed above, forms into a multijet structure. Once the growth is halted, and the enstrophy settles into equilibrium, quasigeostrophic turbulence causes the mean horizontal scales to increase. The inverse energy cascade also affects the jets and the initial multijet structure (which so far was determined only by the dominant growing mode) breaks down; then fewer but stronger jets appear (Fig. 10).

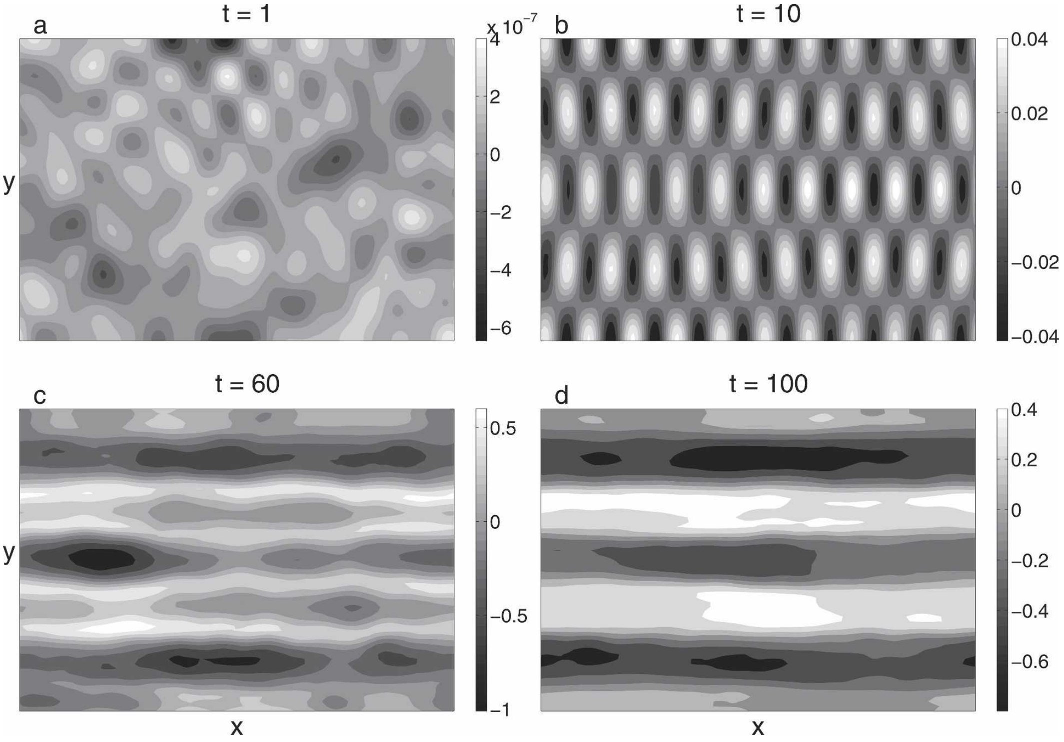

FIG. 6. Instantaneous total zonal velocity fields at different times for the top layer (run S5). Beginning with (a) a random vorticity perturbation, the flow then becomes (b) baroclinically unstable dominated by the fastest growing mode (in this case $k_m = 10$, $l_m = 4$), then (c) several jets are formed matching the prediction of the truncated model, and (d) they cascade to stable jets with a typical width on the order of the Rhines scale. (Full simulations of the zonal velocity field for this run are available as an electronic supplement: doi:10.1175/JAS4009.s1; and also online at http://lake.mit.edu/~glenn/yohai/jets/jas07.htm.)

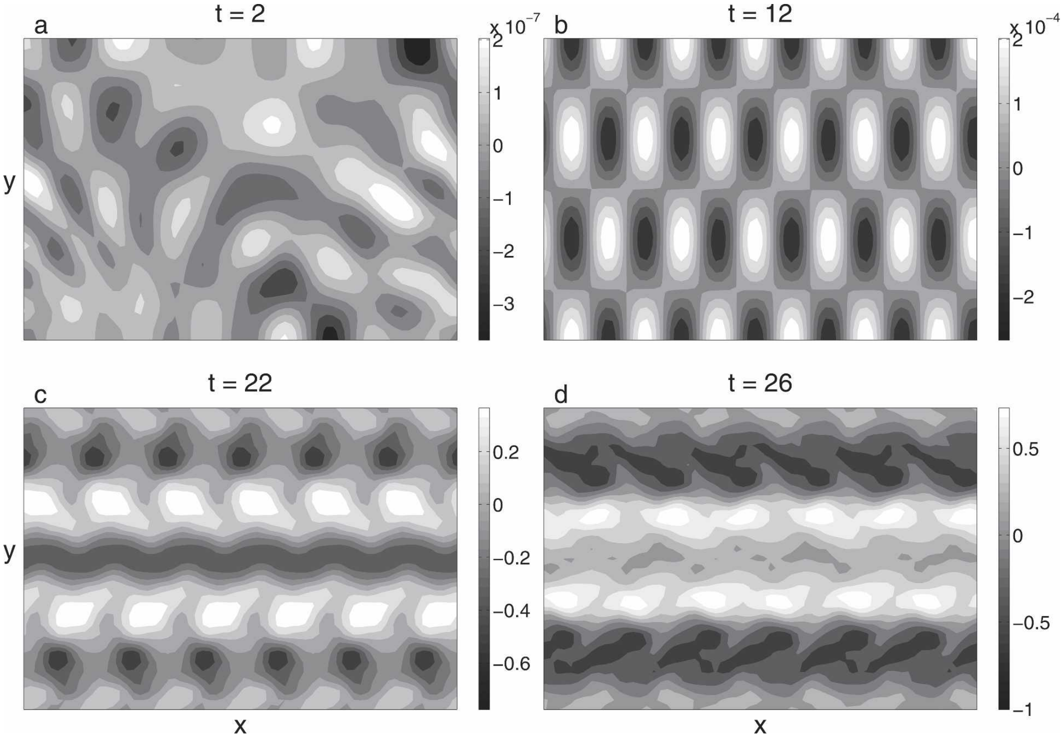

FIG. 7. The transition from baroclinic instability to jets: Instantaneous total zonal velocity fields at different times for the top layer. These snapshots zoom in on the transition from the growing baroclinic perturbation to jets; (a) beginning from a weak random eddy field, (b) to a growing baroclinic perturbation, and (c) transitioning to (d) a jet structure cascading to larger meridional scales. (Full simulations of the zonal velocity field for this run and the streamfunction and potential vorticity fields for both layers are available as an electronic supplement: doi:10.1175/JAS4009.s1; and also online at http://lake.mit.edu/~glenn/yohai/jets/jas07.htm.)

An example of the formation of jets is presented in Fig. 6, which shows snapshots of the zonal velocity field of the top layer (without the constant applied velocity U_1 to emphasis the change of the amplitude following the instability) at different times. Initially a small random perturbation is applied to the basic state (Fig. 6a). At some time the fastest growing mode (in this case $k_m = 10$, $l_m = 4$) becomes dominant (Fig. 6b) and the perturbation grows exponentially. Then, as predicted by the truncated model, the nonlinear interactions form several jets (Fig. 6c). In time, more modes come in, the flow becomes turbulent, and an inverse energy cascade begins setting five major jets (Fig. 6d) in the channel (two eastward and three westward) with a typical width (Fig. 8) on the order of the Rhines scale (Figure 9 includes arrows for the total velocity for the same run (S5), indicating the dominance of the zonal velocities over the meridional velocities). Figure 7 shows a similar plot but for a case of higher vertical shear, which grows in a lower wavenumber ($k_m = 6$, $l_m = 3$) and cascades rather quickly into five jets and then one wide central eastward jet with two narrower westward jets. The snapshots in this case are closer in time and show the transition from a linearly growing disturbance into a strong zonal jet.

Geostrophic turbulence theory predicts that after the system becomes turbulent the typical scale will cascade up to the Rhines scale $L_\beta = \pi\sqrt{(2U/\beta)}$ (Rhines 1975). The relation of this scale to the meridional scale of the Jovian jets has been proposed by Williams (1979). It can be seen in Table 1 that our numerical results agree with this scaling, since the lower the shear, the higher the mode of the fastest growing mode might be, and then more initial jets may be formed. Typically, more jets at the initial stages result in more jets at equilibrium after the inverse energy cascade. Figure 8 shows the mean typical scale of the jets as function of the shear for all standard runs (some presented in Table 1). The width of the jet is determined by doing a spectral analysis of the final statistical steady state for each run and averaging the leading meridional wavelength across the channel. We can see that in general the final scale is governed by the Rhines scale.

Figure 9 shows the final zonal state for a few of the experiments shown in Table 1. The experiments differ in the applied shear, which sets a different induced me-

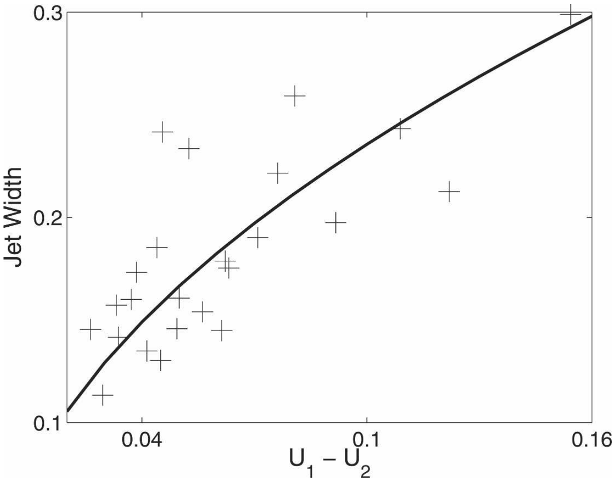

FIG. 8. The jet width as a function of the applied shear. The marks denote the average width of the jets in the top layer for each standard run. The width of the jet is determined by a spectral analysis of the final statistical steady state, and averaging the leading meridional wavelength across the channel. The solid line is the theoretical value for the Rhines scale using the nondimensional shear and the β value for the upper layer.

ridional structure resulting in a different statistical steady state after the energy cascade. The arrows (which follow the streamfunction) show the dominance of the zonal velocities over the meridional ones.

In all experiments the nonlinear correction $\overline{U_n}$, which is initially weak (due to the small initial amplitude) grows substantially to the order of the basic flow. This induced zonal velocity always has a multijet structure, and therefore since the basic flow is always constant the emergence of the jets depends on the amplitude ratio between the eddy zonal velocity and the induced zonal velocity. To quantify the strength of the jets we define a parameter η for each layer, as the ratio of the mean of the $\overline{U_n}$ field to the mean of the eddy field u' averaged over time

$$\eta_n = \left(\frac{\langle \overline{U_n}^2 \rangle}{\langle u_n'^2 \rangle}\right)^{1/2}. \tag{33}$$

Therefore a $\eta > 1$ value is a flow dominated by the jets while a $\eta < 1$ value is a flow dominated by eddies. The η values for both layers in different runs are given in

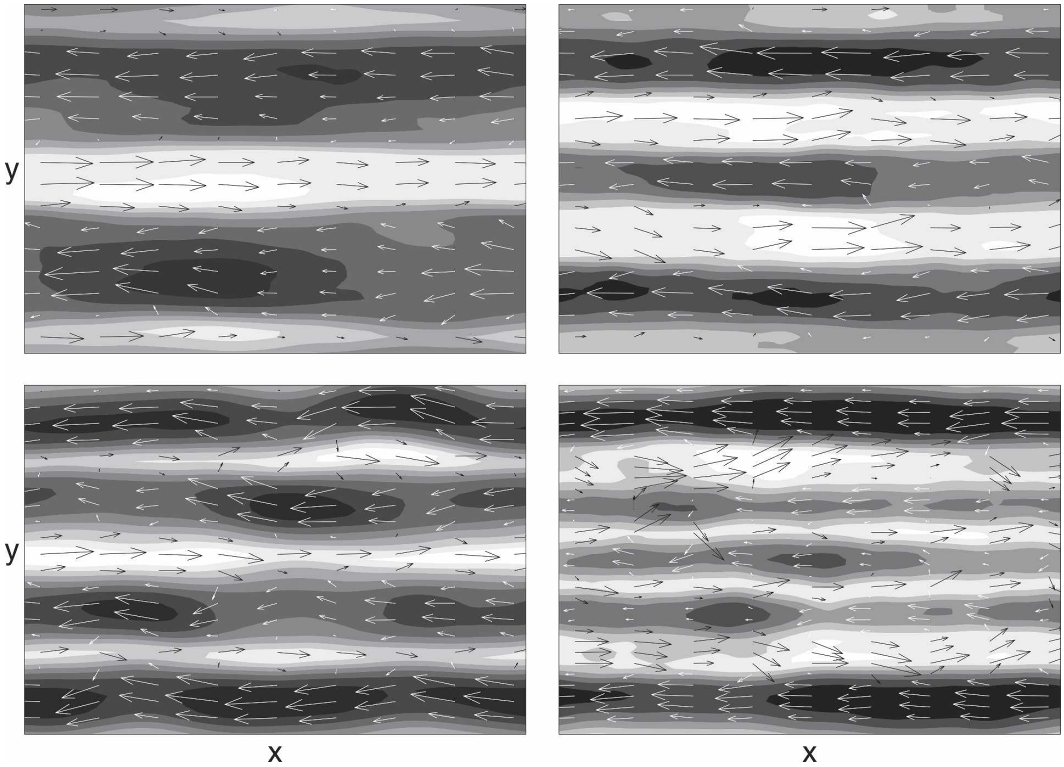

FIG. 9. Snapshots of the steady-state total velocity fields for different runs. The contours are the zonal velocity and arrows show the total velocity (zonal and meridional). (upper left) Run S13 with an applied shear of $U_S = 0.0525$ and fastest growing mode $k_m = 10$, $l_m = 8$; (upper right) run S5 with an applied shear of $U_S = 0.0372$ and fastest growing mode k_m, $l_m = 10, 4$; (lower left) run S14 with an applied shear of $U_S = 0.0562$ and fastest growing mode k_m, $l_m = 8, 4$; (lower right) run F2 ($\delta = 0.1$) with an applied shear of $U_S = 0.037$ and fastest growing mode k_m, $l_m = 9, 7$. (Full simulations from a random perturbation to this steady state for each run is available as an electronic supplement: doi.10.1175/JAS4009.s1; and also online at http://lake.mit.edu/~glenn/yohai/jets/jas07.htm.)

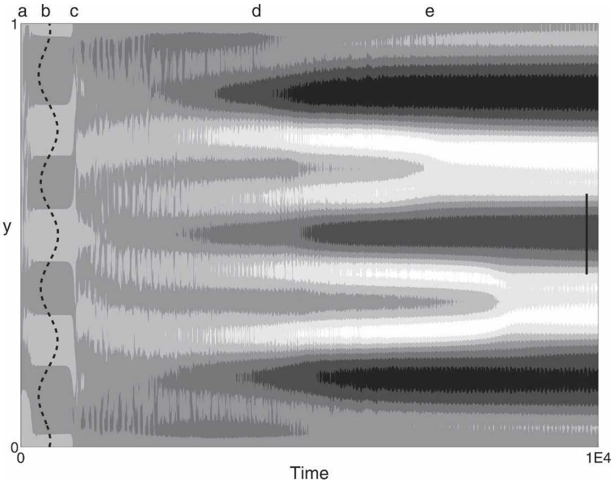

FIG. 10. The evolution of the induced zonal flow of the top layer $\overline{U_1}$ in time. It begins from a weak random field (a) until the fastest growing mode picks up. (b) As this mode grows, an induced meridionally varying flow emerges matching the prediction of the truncated model for $\overline{U_C}$ (superimposed by the dashed line), until the nonlinearities become big enough that more modes come in. (c) Then the flow becomes turbulent; and (d) the jets become less organized, diverging from the initial structure of Eq. (29). The jet meridional scale increases to the Rhines scale (shown by the solid line on the right), leaving the system with five jets (e). Once it reaches the Rhines scale the induced zonal flow remains stable. A longer time of the same run (S5) can be seen in the bottom panel of Fig. 11.

Table 1. An example for the evolution of the induced zonal velocity $\overline{U_1}$ in time is given in Fig. 10.

Alternatively, it is useful to look at the kinetic energy of the eddies and the mean. Figure 11 shows these kinetic energies as a function of time in both layers. Because the induced flow is a consequence of eddy interaction, the mean kinetic energy is smaller than the eddy kinetic energy in the initial stages. However once geostrophic turbulence takes over and the energy cascades to larger scales, the kinetic energy is transferred to the mean and the mean zonal flow dominates over the eddy field. In the bottom deep layer however the energy remains in the eddy field, meaning that for this time scale, the flow does not become barotropic and the jets are concentrated in the upper layer.

6. Discussion

In all numerical results shown above, the jets are seen in snapshots of the total velocity field without applying zonal or time averaging. We find that when we use such averaging as is often done in studies of jets (cf. Panetta 1993) even stronger jets seem to be created and with a bigger η value, yet in some of these cases the instantaneous eddy field u_n' is actually dominant over the $\overline{U_n}$ field ($\eta \ll 1$), and the snapshot plots seem not to resemble jets. This is often the case in the deep layer where the averaged induced zonal velocity $\overline{U_2}$ is smaller than $\overline{U_1}$ by a factor of $1/\delta$ (32). In the top layer, however, whatever the applied shear, there is an induced zonal flow that is typically at least as strong as the eddy field ($\eta > 1$). This can be seen in Table 1 where in addition to the standard run showing the relation between the applied shear and the number of jets (Fig. 8), sensitivity studies to the ratio of β's and layer depths are given. We find that the bigger the absolute value of the negative β, the more jets exist in the top layer (due to the equivalence to weaker shear—Fig. 1), and the bigger the depth ratio the weaker is the induced zonal velocity in the bottom layer, while the top layer is dominated by jets.

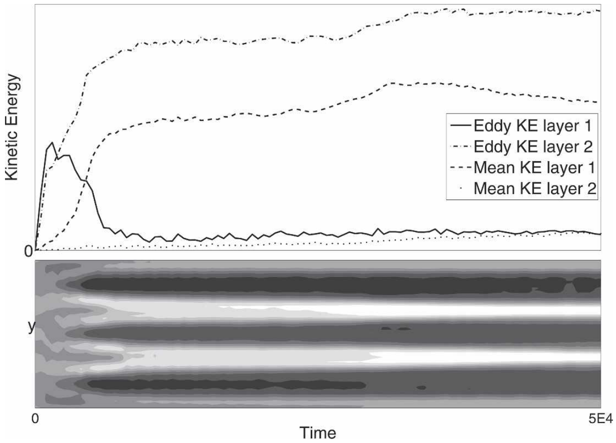

FIG. 11. (top) The kinetic energy for the induced velocity field $\overline{U_n}$ and the eddy field u_n' for both layers as a function of time (run S5). (bottom) The corresponding evolution of the induced zonal velocity $\overline{U_1}$ in time across the channel.

Figure 12 shows on the left-hand side panels the instantaneous picture after the system has reached steady state and on the right side panels the corresponding temporally averaged velocity. The upper panels (run S3, $\eta_1 = 3.1$) features four westward jets and three eastward jets in the snapshot plot, and indeed the time mean figure on the right shows the same meridional structure with similar amplitudes. The middle panels (run S1, $\eta_1 = 1.87$) shows a case with a field showing some jets but within an obvious eddy field, while the time-average plot shows distinct jets. The bottom panels show a case where the zonal velocity field is dominated by large eddies (bottom layer of run S13, $\eta_2 = 0.28$) without any jets, yet when averaged the eddies disappear, leaving only the induced zonal velocity, which gives an appearance of a strong meridional variation and a jet structure. Therefore we emphasis that in this work we do not need to perform such averaging to the velocity field, and the jets appear in the instantaneous picture. In the observations of the Jovian planets

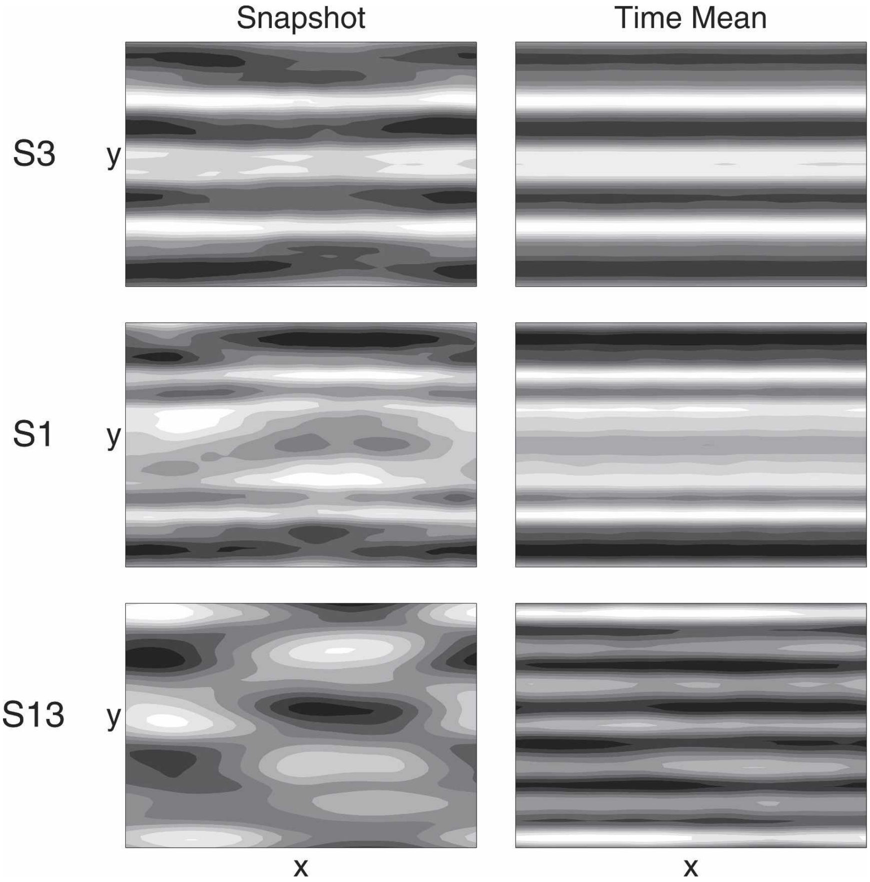

FIG. 12. Comparison of the instantaneous and time-mean, steady-state, total zonal velocity field for different cases. (upper) A case (S3) where the time mean represents well the instantaneous field; (middle) a case (S1) where the instantaneous field shows some jets but also strong eddies that do not appear in the time mean, and (bottom) a case (bottom layer of S13) where the instantaneous picture is totally dominated by big eddies while the averaged picture gives an appearance of a strong meridional variation.

the flow field is established by tracking cloud features, and therefore we expect the instantaneous picture to be most closely related to the data.

The main caveat to keep in mind regarding the model we used here is the assumed baroclinic structure, which although converted from the standard terrestrial case based on estimates of Ingersoll and Pollard (1982), still is quasigeostrophic, a questionable approximation for deep atmospheres. However, assuming baroclinicity does play a role in the dynamics, and given the *Galileo* observations of Jupiter that imply that there is an upper nonconvective layer (Atkinson et al. 1996; Seiff et al. 1996) resembling a terrestrial weather layer, then this model may give some insight to the mechanism driving the Jovian jets. Of course there is much more to be desired in terms of observations of the outer planet's atmospheres in order to develop theoretical understanding of the deep columnar structure.

One of the main questions arising from observations on Jupiter and Saturn is that from the data it seems that the barotropic stability condition is violated (Ingersoll et al. 1981; Smith et al. 1982; Stamp and Dowling 1993), yet the jets seem stable in time. Barotropic instability in a single-beta model, whether one or two layers, is very efficient and eliminates such gradients quickly. Thus, previous barotropic models featuring stable jets had to have this inconsistency with the data. Ingersoll and Pollard (1982) resolve this problem by suggesting an alternative stability criterion due to the internal columnar structure. They suggest that in order for the fluid to have stable jets β should be bigger than $-u_{yy}/3$. Their analysis is consistent with the Voyager data. In our model, because of the special geometry used for the bottom convective layer, which results in a scale separation between the scale of the instability and the resulting jets, the barotropic stability condition is still vio-

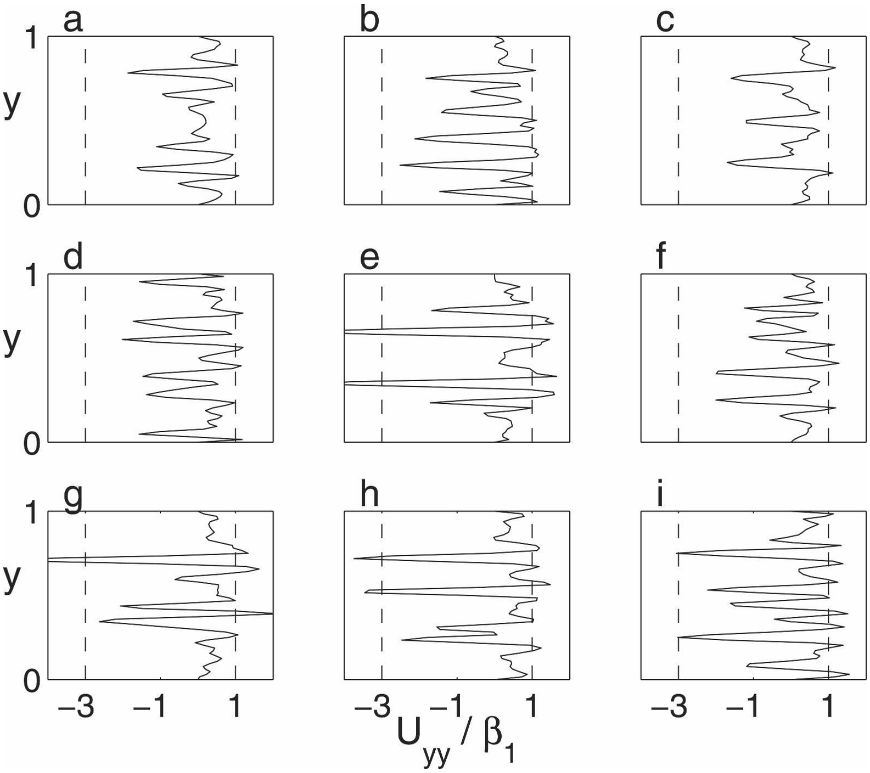

FIG. 13. The u_{yy}/β_1 curve as function of the width of the channel for some of the runs [(a) S1, (b) S2, (c) S3, (d) S5, (e) S13, (f) S4, (g) S8, (h) S9, (i) B2]. The dashed line on the right is the standard barotropic stability criterion, and the dashed line on the left is the one suggested by Ingersoll and Pollard (1982). In most cases the curve crosses the barotropic stability curve several times, similar to what is seen in the observations.

lated (Fig. 13). Yet the jets are stable in time, because of the continuing exchange of energy between the mean flow and the eddies and the influence of the deep layer on the upper-layer flows [in the spirit of Stamp and Dowling (1993), but with jets that are less barotropic]. We note that the upper layer u_{yy} appears to approach β_2 on the negative side, indicating again the importance of the coupling between the layers.

7. Conclusions

Traditionally there have been two hypotheses for the existence of the jets observed on the giant planets. One approach (Busse 1976) assumed that the interior is barotropic and the jets are generated by an internal columnar structure, while the other approach treats the gas planets as a shallow water system (Dowling and Ingersoll 1989) assuming the deep atmosphere is passive and jets can emerge from eddy interactions (Cho and Polvani 1996; Williams 1979). Recent observations (Atkinson et al. 1996; Porco et al. 2003) imply that taking only one of these approaches may be omitting important components of the dynamics. In this work we tried to combine these two approaches assuming a baroclinic structure, which internally is dominated by columnar structures interacting with an upper layer resembling a regular weather type layer. In addition, we propose that baroclinic instability may provide the energy source, even in the limit of weak vertical shear as suggested by observations.

We show an analytic solution for the generation of jets in the limit of a single mode perturbation interacting with baroclinic zonal flows and then proceed using a pseudospectral fully nonlinear numerical model to show that such jets can be generated by baroclinic instability. The analytical solution provides useful insight into the mechanism observed in the numerical results, especially in the way nonlinearity organizes the zonal flow field. The obtained jets are stable on long time scales and are visible in the instantaneous spatial numerical picture without the need for zonal or time averaging. Clearly there is much more to be understood in the dynamics acting in the interior of such gas giants, and our parameterization of the interior is just a first step. However it does suggest the importance of coupling these two regimes even though they may be governed by very different physical mechanisms.

Acknowledgments. We thank Joseph Pedlosky and Eli Tziperman for some very helpful discussions during the preparation of this work. We thank F. M. Flasar and an anonymous reviewer for their careful analysis and constructive comments. This work was supported by an NSF Grant OCE-0137023.

APPENDIX

Derivation of the Truncated Model

In this appendix we derive the nonlinear solution for the truncated model. We begin by rewriting the barotropic and baroclinic perturbation equations using Q_T and Q_C as defined by (18) and (19).

$$\frac{\partial}{\partial t}q_T + U_C\frac{\partial}{\partial x}q_C + Q_T\frac{\partial}{\partial x}\phi_T + Q_C\frac{\partial}{\partial x}\phi_C + J(\phi_T, q_T) + J(\phi_C, q_C) = 0 \tag{A1}$$

$$\frac{\partial}{\partial t}q_C + U_C\left(\frac{\partial}{\partial x}q_T + \xi\frac{\partial}{\partial x}q_C\right) + Q_T\frac{\partial}{\partial x}\phi_C + Q_C\left(\frac{\partial}{\partial x}\phi_T + \xi\frac{\partial}{\partial x}\phi_C\right) + J(\phi_T + \xi\phi_C, q_C) + J(\phi_C, q_T) = 0. \tag{A2}$$

Expressing the perturbation potential vorticity as a single perturbation wave (22), (23) and using the inversion relations (24), (25) for the streamfunctions, we find that the Jacobians in the barotropic equations vanish while the ones in the baroclinic equations give an expression of the form

$$\overline{q_C} = \overline{q'_C}(t)\sin(2ly) \tag{A3}$$

as given by (26). Using the inversion relation (28) and the boundary condition (8) gives an expression for the correction to the basic streamfunction given by

$$\overline{\phi_C} = \frac{-\overline{q'_C}(t)}{4l^2 + F_1 + F_2} \times \left\{ \sin(2ly) - \frac{\sinh\left[\sqrt{F_1 + F_2}\left(y - \frac{1}{2}\right)\right]}{\sqrt{F_1 + F_2}\cosh\left(\frac{\sqrt{F_1 + F_2}}{2}\right)} \right\}, \tag{A4}$$

which when differentiated in y gives a correction to the mean zonal velocity as given in (29). Now we rewrite the barotropic and baroclinic perturbation Eqs. (A1), (A2) using (22), (23), and (A3). For clarity we note that the baroclinic basic zonal flow now has the form

$$U_C = U_0 + \overline{U_C} \equiv U_0 + \overline{q'_C}(t)f_u(y), \tag{A5}$$

where the structure function f_u is defined by (29), and the baroclinic potential vorticity gradient will now also include the correction from the induced mean flow. Then (A1), (A2) become

$$\sin(ly)\frac{\partial}{\partial t}q'_T + ik\sin(ly)\left\{(U_0 + \overline{q'_C}f_u)q'_C - Q_T\frac{q'_T}{\kappa^2} - [Q_C + 2l\overline{q'_C}\cos(2ly)]\frac{q'_C}{\kappa^2 + F_1 + F_2}\right\} = 0 \tag{A6}$$

$$\begin{aligned}
&\frac{\partial}{\partial t}[\sin(ly)q'_C + \sin(2ly)q'_C] + \\
&\qquad ik\sin(ly)\left\{(U_0 + \overline{q'_C}f_u)(q'_T + \xi q'_C) - Q_T\frac{q'_C}{\kappa^2 + F_1 + F_2} - [Q_C + 2l\overline{q'_C}\cos(2ly)]\left(\frac{q'_T}{\kappa^2} + \frac{\xi q'_C}{\kappa^2 + F_1 + F_2}\right)\right\} \\
&\quad + \frac{ikl\sin(2ly)(F_1 + F_2)}{\kappa^2(\kappa^2 + F_1 + F_2)}(q'_C q'^{*}_T - q'^{*}_C q'_T) = 0.
\end{aligned} \tag{A7}$$

Multiplying by sin(ly), integrating over the channel and normalizing by $\int \sin(ly)^2\,dy$ gives

$$\frac{\partial}{\partial t} q'_T + ik\left[(U_0 + \overline{q'_C} I_u) q'_C - Q_T \frac{q'_T}{\kappa^2} - (Q_C - l\overline{q'_C}) \frac{q'_C}{\kappa^2 + F_1 + F_2}\right] = 0 \tag{A8}$$

$$\frac{\partial}{\partial t} q'_C + ik\left[(U_0 + \overline{q'_C} I_u)(q'_T + \xi q'_C) - Q_T \frac{q'_C}{\kappa^2 + F_1 + F_2} - (Q_C - l\overline{q'_C})\left(\frac{q'_T}{\kappa^2} + \frac{\xi q'_C}{\kappa^2 + F_1 + F_2}\right)\right] = 0 \tag{A9}$$

where I_u is defined as

$$I_u = \frac{-l}{4l^2 + F_1 + F_2} \times \left[1 + \frac{16l^3 \tanh\left(\dfrac{\pi\sqrt{F_1 + F_2}}{2l}\right)}{\pi\sqrt{F_1 + F_2}(4l^2 + F_1 + F_2)}\right] \tag{A10}$$

while projecting by sin($2ly$) gives an equation for the baroclinic mean correction

$$\frac{\partial}{\partial t} \overline{q'_C} + \frac{ikl(F_1 + F_2)}{\kappa^2(\kappa^2 + F_1 + F_2)} (q'_C q'^*_T - q'^*_C q'_T) = 0. \tag{A11}$$

Equations (A8), (A9), and (A11) define the system which we can solve for q'_T, q'_C and $\overline{q'_C}$. We rewrite the equation for the perturbation (A8) and (A9) in the form

$$\frac{\partial}{\partial t} \mathbf{q} + ik\mathbf{L}\mathbf{q} + ik\overline{q'_C}\mathbf{N}\mathbf{q} = 0, \tag{A12}$$

where $\mathbf{q} = \begin{pmatrix} q'_T \\ q'_C \end{pmatrix}$, and the operators are

$$\mathbf{L} = \begin{pmatrix} -\dfrac{Q_T}{\kappa^2} & U_0 - \dfrac{Q_C}{\kappa^2 + F_1 + F_2} \\ U_0 - \dfrac{Q_C}{\kappa^2} & \xi U_0 - \dfrac{Q_T + \xi Q_C}{\kappa^2 + F_1 + F_2} \end{pmatrix} \tag{A13}$$

$$\mathbf{N} = \begin{pmatrix} 0 & \mathbf{I}_u + \dfrac{l}{\kappa^2 + F_1 + F_2} \\ \mathbf{I}_u + \dfrac{l}{\kappa^2} & \xi\mathbf{I}_u + \dfrac{\xi l}{\kappa^2 + F_1 + F_2} \end{pmatrix}. \tag{A14}$$

The limit where $\mathbf{N} = 0$ gives back the linear problem.

REFERENCES

Atkinson, D. H., J. B. Pollack, and A. Seiff, 1996: Galileo Doppler measurements of the deep zonal winds at Jupiter. *Science,* **272,** 842–843.

Aurnou, J. M., and P. L. Olson, 2001: Strong zonal winds from thermal convection in a rotating spherical shell. *Geophys. Res. Lett.,* **28,** 2557–2559.

Boyd, J. P., 2001: *Chebyshev and Fourier Spectral Methods.* 2d ed. Dover, 668 pp.

Busse, F. H., 1970: Thermal instabilities in rapidly rotating systems. *J. Fluid Mech.,* **44,** 441–460.

——, 1976: A simple model of convection in the Jovian atmosphere. *Icarus,* **29,** 255–260.

——, 1994: Convection driven zonal flows and vortices in the major planets. *Chaos,* **4** (2), 123–134.

Cho, J., and L. M. Polvani, 1996: The formation of jets and vortices from freely-evolving shallow water turbulence on the surface of a sphere. *Phys. Fluids,* **8,** 1531–1552.

Christensen, U. R., 2002: Zonal flow driven by strongly supercritical convection in rotating spherical shells. *J. Fluid Mech.,* **470,** 115–133.

Conrath, B. J., F. M. Flasar, J. A. Pirraglia, P. J. Gierasch, and G. E. Hunt, 1981: Thermal structure and dynamics of the Jovian atmosphere. II—Visible cloud features. *J. Geophys. Res.,* **86,** 8769–8775.

Dowling, T. E., and A. P. Ingersoll, 1989: Jupiter's Great Red Spot as a shallow water system. *J. Atmos. Sci.,* **46,** 3256–3278.

Flierl, G. R., 1992: Deep jets and shallow spots. Geophysical Fluid Dynamics summer study program. Woods Hole Oceanographic Institution Tech. Rep. WHOI-93-24, 432 pp.

Galperin, B., S. Sukoriansky, and H.-P. Huang, 2001: Universal n-5 spectrum of zonal flows on giant planets. *Phys. Fluids,* **13,** 1545–1548.

——, ——, P. Read, Y. Yamazaki, and R. Wordsworth, 2006: Anisotropic turbulence and zonal jets in rotating flows with a beta effect. *Nonlinear Proc. Geophys.,* **13,** 83–98.

Gierasch, P. J., J. A. Magalhaes, and B. J. Conrath, 1986: Zonal mean properties of Jupiter's upper troposphere from Voyager infrared observations. *Icarus,* **67,** 456–483.

Guillot, T., 1999: Interiors of giant planets inside and outside the solar system. *Science,* **286,** 72–77.

Hanel, R. A., B. J. Conrath, L. Herath, V. Kunde, and J. Pirraglia, 1981: Albedo, internal heat, and energy balance of Jupiter—Preliminary results of the Voyager infrared investigation. *J. Geophys. Res.,* **86,** 8705–8712.

——, ——, V. G. Kunde, J. C. Pearl, and J. A. Pirraglia, 1983: Albedo, internal heat flux, and energy balance of Saturn. *Icarus,* **53,** 262–285.

Heimpel, M., J. Aurnou, and J. Wicht, 2005: Simulation of equatorial and high-latitude jets on Jupiter in a deep convection model. *Nature,* **438,** 193–196.

Huang, H.-P., and W. A. Robinson, 1998: Two-dimensional turbulence and persistent zonal jets in a global barotropic model. *J. Atmos. Sci.,* **55,** 611–632.

——, B. Galperin, and S. Sukoriansky, 2001: Generation of mean flows and jets on a beta plane and over topography. *Phys. Fluids,* **13,** 225–240.

Ingersoll, A. P., 1976: Pioneer 10 and 11 observations and the dynamics of Jupiter's atmosphere. *Icarus,* **29,** 245–252.

——, 1990: Atmospheric dynamics of the outer planets. *Science,* **248,** 308–315.

——, and D. Pollard, 1982: Motion in the interiors and atmospheres of Jupiter and Saturn: Scale analysis, anelastic equations, barotropic stability criterion. *Icarus,* **52,** 62–80.

——, R. F. Beebe, J. L. Mitchell, G. W. Garneau, G. M. Yagi, and J.-P. Muller, 1981: Interaction of eddies and mean zonal flow on Jupiter as inferred from Voyager 1 and 2 images. *J. Geophys. Res.,* **86,** 8733–8743.

Kuo, H. L., 1949: Dynamic instability of two-dimensional nondivergent flow in a barotropic atmosphere. *J. Meteor.,* **6,** 105–122.

Lee, S., 2005: Baroclinic multiple zonal jets on a sphere. *J. Atmos. Sci.,* **62,** 2484–2498.

Manifori, A. J., and W. R. Young, 1999: Slow evolution of zonal jets on the beta plane. *J. Atmos. Sci.,* **56,** 784–800.

Manneville, J. B., and P. Olson, 1996: Banded convection in rotating fluid spheres and the circulation of the Jovian atmosphere. *Icarus,* **122,** 242–250.

Panetta, R. L., 1993: Zonal jets in wide baroclinically unstable regions: Persistence and scale selection. *J. Atmos. Sci.,* **50,** 2073–2106.

Pearl, J. C., and B. J. Conrath, 1991: The albedo, effective temperature, and energy balance of Neptune, as determined from Voyager data. *J. Geophys. Res.,* **96,** 18 921–18 930.

Pedlosky, J., 1970: Finite-amplitude baroclinic waves. *J. Atmos. Sci.,* **27,** 15–30.

——, 1987: *Geophysical Fluid Dynamics.* Springer-Verlag, 710 pp.

Phillips, N. A., 1954: Energy transformations and meridional circulations associated with simple baroclinic waves in a two level quasi-geostrophic model. *Tellus,* **6,** 273–286.

Porco, C. C., and Coauthors, 2003: Cassini imaging of Jupiter's atmosphere, satellites and rings. *Science,* **299,** 1541–1547.

——, and Coauthors, 2005: Cassini imaging science: Initial results on Saturn's atmosphere. *Science,* **307,** 1243–1247.

Rhines, P. B., 1975: Waves and turbulence on a beta plane. *J. Fluid Mech.,* **69,** 417–443.

——, 1979: Geostrophic turbulence. *Annu. Rev. Fluid Mech.,* **11,** 401–441.

Robinson, A. R., and J. McWilliams, 1974: The baroclinic instability of the open ocean. *J. Phys. Oceanogr.,* **4,** 281–294.

Seiff, A., and Coauthors, 1996: Structure of the atmosphere of Jupiter: Galileo probe measurements. *Science,* **272,** 844–845.

Smith, B. A., and Coauthors, 1982: A new look at the Saturn system: The Voyager 2 images. *Science,* **215,** 505–537.

Smith, K. S., 2004: A local model for planetary atmospheres forced by small-scale convection. *J. Atmos. Sci.,* **61,** 1420–1433.

Stamp, A. P., and T. E. Dowling, 1993: Jupiter's winds and Arnol'd's second stability theorem: Slowly moving waves and neutral stability. *J. Geophys. Res.,* **98,** 18 847–18 855.

Steinsaltz, D., 1987: Instability of baroclinic waves with bottom slope. *J. Phys. Oceanogr.,* **17,** 2343–2350.

Sun, Z.-P., G. Schubert, and G. A. Glatzmaier, 1993: Banded surface flow maintained by convection in a model of the rapidly rotating giant planets. *Science,* **260,** 661–664.

Vallis, G. K., and M. E. Maltrud, 1993: Generation of mean flows and jets on a beta plane and over topography. *J. Phys. Oceanogr.,* **23,** 1346–1362.

Williams, G. P., 1978: Planetary circulations: 1. Barotropic representation of Jovian and terrestrial turbulence. *J. Atmos. Sci.,* **35,** 1399–1426.

——, 1979: Planetary circulations: 2. The Jovian quasi-geostrophic regime. *J. Atmos. Sci.,* **36,** 932–969.

——, 2003: Jovian dynamics. Part III: Multiple, migrating, and equatorial jets. *J. Atmos. Sci.,* **60,** 1270–1296.

Yano, J. I., 2005: Origins of atmospheric zonal winds. *Nature,* **421,** 36.

——, and G. R. Flierl, 1994: Jupiter's Great Red Spot: Compactness condition and stability. *Ann. Geophys.,* **12,** 1–18.

Zhang, K., and G. Schubert, 1996: Penetrative convection and zonal flow on Jupiter. *Science,* **273,** 941–943.

——, and ——, 1997: Linear penetrative spherical rotating convection. *J. Atmos. Sci.,* **54,** 2509–2518.